Article

Effects of Solvent Diols on the Synthesis of ZnFe$_2$O$_4$ Particles and Their Use as Heterogeneous Photo-Fenton Catalysts

Chayene Gonçalves Anchieta [1], Adriano Cancelier [1], Marcio Antonio Mazutti [1], Sérgio Luiz Jahn [1], Raquel Cristine Kuhn [1], Andre Gündel [2], Osvaldo Chiavone-Filho [3] and Edson Luiz Foletto [1,*]

[1] Department of Chemical Engineering, Federal University of Santa Maria, 97105-900 Santa Maria, Brazil; E-Mails: chayeneanchieta@gmail.com (C.G.A.); adriano.cancelier@ufsm.br (A.C.); mazutti@ufsm.br (M.A.M.); jahn@smail.ufsm.br (S.L.J.); raquel.kuhn@ufsm.br (R.C.K.)

[2] Department of Physics, Federal University of Pampa, 96413-170 Bagé, Brazil; E-Mail: andre.gundel@unipampa.edu.br

[3] Department of Chemical Engineering, Federal University of Rio Grande do Norte, 59066-800 Natal, Brazil; E-Mail: osvaldo@eq.ufrn.br

* Author to whom correspondence should be addressed; E-Mail: foletto@smail.ufsm.br or efoletto@gmail.com; Tel.: +55-55-3220-8448; Fax: +55-55-3220-8030.

Abstract: A solvothermal method was used to prepare zinc ferrite spinel oxide (ZnFe$_2$O$_4$) using ethylene glycol and 1,4 butanediol as solvent diols, and the influence of diols on the physical properties of ZnFe$_2$O$_4$ particles was investigated. The produced particles were characterized by X-ray powder diffraction (XRD), atomic force microscopy (AFM), Fourier transform infrared spectroscopy (FTIR) and nitrogen adsorption isotherms, and the catalytic activity for the organic pollutant decomposition by heterogeneous photo-Fenton reaction was investigated. Both solvents produced particles with cubic spinel structure. Microporous and mesoporous structures were obtained when ethylene glycol and 1,4 butanediol were used as diols, respectively. A higher pore volume and surface area, as well as a higher catalytic activity for the pollutant degradation were found when 1,4 butanediol was used as solvent.

Keywords: zinc ferrite; ZnFe$_2$O$_4$; synthesis; solvothermal; photo-Fenton

1. Introduction

Zinc ferrite ($ZnFe_2O_4$) is a spinel oxide that possesses excellent magnetic and electrical properties [1,2], as well as excellent chemical and thermal stabilities [3]. $ZnFe_2O_4$ oxide has received much attention due to its potential applications in detecting gases [4], as an adsorbent material for hot-gas desulfurization [5], in biomedicine [6], for its magnetic, optical and electrical behaviors [7–11] and catalytic application [12,13]. Recently, zinc ferrite has been used as an efficient heterogeneous Fenton catalyst in degrading organic pollutants from an aqueous solution [14–16]. $ZnFe_2O_4$ nanoparticles were developed as a catalyst for the degradation of benzotriazole by a heterogeneous photoelectron-Fenton process and have shown to be highly efficient for benzotriazole degradation [16]. A hydrothermal method was used to synthesize $ZnFe_2O_4$ powders with an average size of 10 nm with the aid of sodium oleate, and they presented good photocatalytic activity in the degradation of Rhodamine B dye under the irradiation of simulated solar light [17]. $ZnFe_2O_4$ film fabricated on a sulfonated silicon substrate via a novel template-assisted route exhibited good photocatalytic activity in the degradation of Rhodamine B under visible light irradiation [18]. $ZnFe_2O_4$ nanocrystallites were synthesized by microwave sintering and played an important role in degrading the methylene blue dye under visible light [19].

$ZnFe_2O_4$ particles have been prepared using various methods, such as co-precipitation [20,21], sol-gel [22], solid-state reaction [23], glycine combustion method [24], combustion reaction using urea as reducing agent [25,26], hydrothermal synthesis [27], solvothermal and microwave-assisted solvothermal synthesis [28], high enegy ball-milling [29], thermal plasma synthesis [30], one-step solid-phase chemical reaction [31], microwave combustion method [32], polyethylene glycol-assisted route [33] and synthesis in supercritical fluids [34,35]. Herein, we report the use of a solvothermal route for the preparation of $ZnFe_2O_4$ particles. A solvothermal route offers advantage over the hydrothermal route, because it does not require the use of surfactants or templates in the reaction medium. The solvothermal method was used to fabricate $ZnFe_2O_4/\alpha\text{-}Fe_2O_3$ composite hollow nanospheres, including polyethylene glycol as template [36]. Li *et al.* [37] and Kuai *et al.* [38] used ethylene glycol as solvent for the synthesis of $ZnFe_2O_4$ nanospheres and Ce^{3+} doped Zn ferrites, respectively.

Accordingly, this work aimed to synthesize $ZnFe_2O_4$ powders with a solvothermal route, using different solvent diols, and to examine their structural properties. In addition, the catalytic performance for organic dye degradation over $ZnFe_2O_4$ powders was investigated.

2. Experimental Section

2.1. Preparation of Powders

The $ZnFe_2O_4$ particles were prepared using the solvothermal method. Zinc nitrate ($Zn(NO_3)_2 \cdot 6H_2O$, analytical grade) and iron nitrate ($Fe(NO_3)_3 \cdot 9H_2O$, analytical grade) were used as zinc and iron sources, respectively, without further purification. Stoichiometric amounts of Zn and Fe nitrates (molar ratio Zn:Fe = 1:2) were used for preparing $ZnFe_2O_4$ powders. Two diols were used was solvent, ethylene glycol ($C_2H_4(OH)_2$, analytical grade) and 1,4 butanediol ($C_4H_{10}O_2$, analytical grade). In a typical synthetic procedure, zinc nitrate (4 mmol) and iron nitrate (8 mmol) were dissolved in 120 mL

of ethylene glycol (EG) and mixed with appropriate amount of sodium acetate (CH$_3$COONa) (60 mmol), under magnetic stirring. Then, the final mixture was charged into a PTFE-lined stainless autoclave, and the solvothermal reaction was carried out at 200 °C for 24 h. Subsequently, the autoclave was left to naturally cool off. The solids were filtered, washed with distilled water, and dried at 110 °C for 10 h to obtain ZnFe$_2$O$_4$-EG. A similar procedure to that described above was carried out using 1,4 butanediol (BD) to obtain ZnFe$_2$O$_4$-DB.

2.2. Characterization of Powders

The XRD patterns were obtained on a Rigaku Miniflex 300 diffractometer with a Cu $K\alpha$ radiation at 30 kV and 10 mA, with a step size (2θ) of 0.03° and a count time of 0.9 s per step. The average size of the ZnFe$_2$O$_4$ spinel crystallite was determined with the Scherrer equation [39]: $D = K \cdot \lambda / (h_{1/2} \cdot \cos\theta)$, where D is the average crystallite size, K the Scherrer constant (0.9), λ the wavelength of incident X-rays (0.1541 nm), $h_{1/2}$ the peak width at half height and θ corresponds to the peak position (in this work, 2θ = 35.36°). The AFM images were obtained by atomic force microscopy (Agilent Technologies 5500 equipment). N$_2$ adsorption-desorption isotherms measurements were carried out at 77 K using an ASAP 2020 apparatus, at a relative pressure (P/P_0) from 0 to 0.99. FTIR spectra were recorded on a Shimadzu IR-Prestige-21 spectrophotometer in the range of 4000–375 cm^{-1}, using pellets prepared by mixing zinc ferrite powder with KBr powder (10 mg zinc ferrite/300 mg KBr).

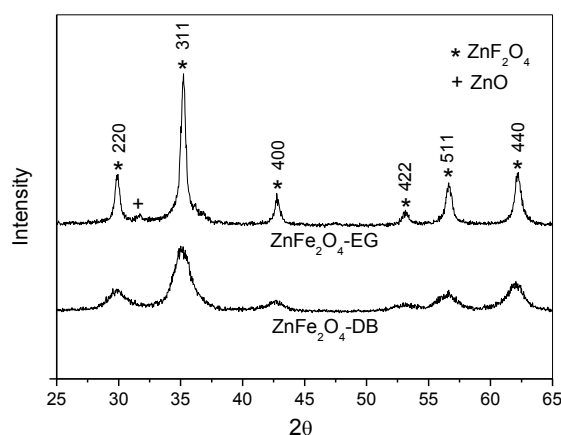## 2.3. Experimental Essays and Reaction Apparatus

A batch–type reactor was used, consisting of a glass tube (internal diameter of 5.0 cm and 6.0 cm in height) with an economic fluorescent lamp (80 W, emit at wavelength above 400 nm) fixed above the reaction solution. Due to the narrow bandgap of ~1.9 eV [37,40], ZnFe$_2$O$_4$ shows a wide absorption in the visible-light region and could be easily excited by visible light, accelerating the degradation of organic molecules from an aqueous solution. Visible light assisted Fenton system for the treatment of dyes has been shown to be very promising [41,42]. The reaction solution was 15 cm apart from the lamp. For the catalytic experiments under visible irradiation, 0.5 g of catalyst was added to 50 mL of Procion Red dye aqueous solution at an initial concentration of 50 mg·L^{-1}, followed by adjusting pH to 3.0 by 0.1 M H$_2$SO$_4$. Acidic conditions (about pH 3) are required for a better performance of Fenton reaction [41,43]. Previous to irradiation, the suspension was magnetically stirred in the dark until reaching the adsorption equilibrium. After the adsorption process, an aliquot of hydrogen peroxide (0.04 mol·L^{-1}) was added to the solution to initiate the reaction. When H$_2$O$_2$ was added, it greatly enhanced the efficiency of degradation, which affects –OH production for the rapid oxidation of contaminants [42,43]. Then the suspension was irradiated by the lamp, and aliquots were collected at set time intervals using a 5 mL syringe, followed by the filtration of the suspension. The reaction was always kept at room temperature. Dye concentration data were treated in the dimensionless form ($C/C_0 = A/A_0$) and plotted as a function of reaction time, where C_0 represents the absorbance of the initial dye solution and C the absorbance of the dye solution at reaction time t. The absorbance was measured using a UV-Vis spectrophotometer (Bel Photonics, SP1105, Bel Photonics do Brasil Ltda., Osasco, Brazil) at maximum wavelength of 543 nm. The concentration of Fe irons leaching from

$ZnFe_2O_4$ particles during the reaction process was measured using atomic absorption spectroscopy (Agilent Technologies, 200 series AA (Agilent Technologies, Inc., Santa Clara, CA, USA).

3. Results and Discussion

Figure 1 shows the XRD patterns of $ZnFe_2O_4$ samples prepared with EG and BD. The diffractograms for both samples indicate that each sample corresponds to a spinel cubic structure according to JCPDS card No. 89-1012. The diffraction peaks at 2θ of 30.05°, 35.36°, 42.78°, 52.96°, 56.78° and 62.2° can be ascribed to the reflection of (220), (311), (400), (422), (511) and (440) planes of the $ZnFe_2O_4$ spinel, respectively. However, a very small amount of ZnO ($2\theta = 31.7$°) was detected in $ZnFe_2O_4$ synthesized with ethylene glycol, as shown in Figure 1. The main difference in the X-ray diffractograms of the $ZnFe_2O_4$ samples prepared with EG and BD is the width of the peaks. It may be noted that the $ZnFe_2O_4$-BD sample has wider peaks than those of $ZnFe_2O_4$-EG. This indicates that the $ZnFe_2O_4$-BD sample has smaller average crystallite size. The average crystallite size calculated by Scherrer equation of nanocrystals synthesized with EG was 24.9 nm, while the average crystallite size of nanocrystals produced with BD was 6.0 nm.

Figure 1. XRD patterns of the samples prepared with different solvent diols.

FTIR spectra of the ferrite samples are presented in Figure 2. The bands at 3440 and 1640 cm^{-1} can be assigned to the stretching vibration mode of adsorbed water molecules on the surface of ferrite crystals [44,45]. However, the main bands that characterize the formation of spinel phase are located at 570 and 440 cm^{-1}, which are associated with the vibrations of Zn-O and Fe-O bonds, respectively [27,44].

Figure 3 shows nitrogen adsorption-desorption isotherms (Figure 3a) of the obtained $ZnFe_2O_4$ samples and their corresponding pore size distribution curves (Figure 3b). As shown in Figure 3, the isotherms, as well as the pore size distribution curves of both samples, are significantly different. The nitrogen adsorption-desorption isotherms (Figure 3a) of the $ZnFe_2O_4$-BD sample are type IV with an H1 hysteresis loop according to the IUPAC classification, which indicates the predominance of mesoporous structure. While those of the $ZnFe_2O_4$-EG sample are of type III, indicating materials with predominantly microporous structure. The size pore distributions (Figure 3b) of the samples confirm the presence of mesoporous for the $ZnFe_2O_4$-BD sample and microporous for the $ZnFe_2O_4$-EG sample. Pore size distribution consisted of one wide peak centered at 150 Å (15 nm) for the $ZnFe_2O_4$-BD sample. This mesoporosity can be attributed to the interparticle pores due to the crystallites

agglomeration. The specific surface area and total pore volume of the $ZnFe_2O_4$-BD sample were 44.6 $m^2 \cdot g^{-1}$ and 0.217 $cm^3 \cdot g^{-1}$ respectively, larger than those of the $ZnFe_2O_4$-EG sample, 14.6 $m^2 \cdot g^{-1}$ and 0.045 $cm^3 \cdot g^{-1}$ respectively. Different values of surface area and pore volume were found when different diols such as ethylene glycol, 1,2 propanediol, 2,3 butanediol and 2-methyl-2,4-pentanediol were used in the preparation of alumina-silica powders using the sol-gel method [46].

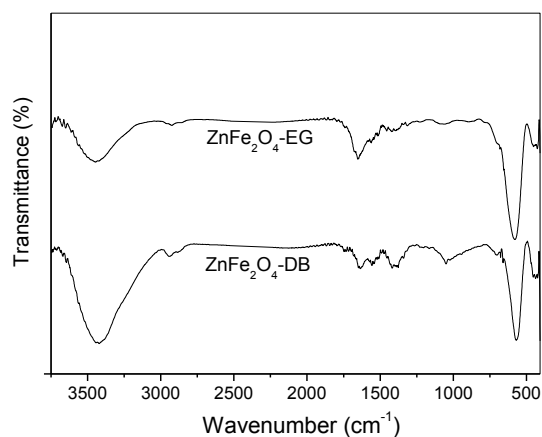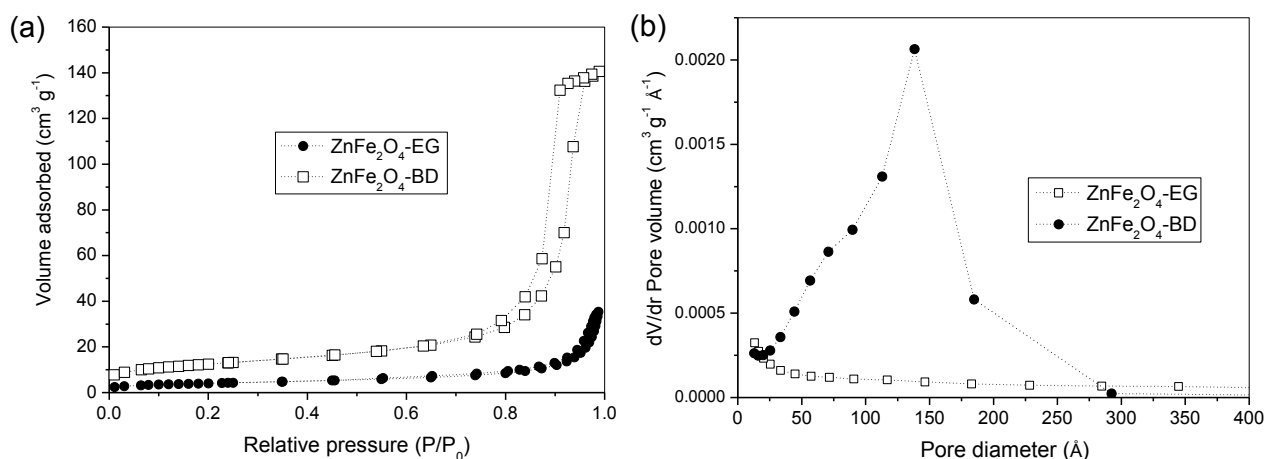**Figure 2.** FTIR spectra of the samples prepared with different solvent diols.

Figure 3. (**a**) N_2 adsorption-desorption isotherms measured at 77 K; and (**b**) pore size distribution curves from the adsorption branches using the BJH method.

AFM images (Figure 4) show that the $ZnFe_2O_4$ samples prepared with EG and BD are formed by the agglomeration of small particles that are smaller than 50 nm, which are on the same order of magnitude of those calculated with the Scherrer equation in XRD analysis.

Preliminary experiments were performed in the conditions of photolysis (with presence of visible light irradiation only) and Fenton reaction (with catalyst and hydrogen peroxide in the absence of visible light irradiation), which negligible results (smaller 5% of dye degradation) were observed for both conditions. In addition, other experiments demonstrated that the dye degradation was negligible when using catalyst in the presence of visible light irradiation and without irradiation. Therefore, the photocatalytic activity of $ZnFe_2O_4$ powders only occurred in the simultaneous presence of visible light irradiation and hydrogen peroxide. Figure 5 depicts the photocatalytic activity of both $ZnFe_2O_4$ samples in the presence of visible light and hydrogen peroxide. $ZnFe_2O_4$-DB particles showed the

highest photocatalytic activity for dye degradation, and complete removal occurred at 30 min of irradiation time, while the efficiency of $ZnFe_2O_4$-EG particles reached 85% of dye degradation at 60 min, as shown in Figure 5a. Thus, it is possible to note that the best catalytic performance occurs in the presence of $ZnFe_2O_4$-DB, and this may be associated with smaller crystallite size and, consequently, higher surface area. Figure 5b illustrates the reaction kinetics for the dye degradation using both catalysts prepared in this present work. The dye degradation followed the pseudo first-order kinetics [47,48] where the reaction rate constants (k) were obtained from slopes of the fit lines of $\ln(C/C_0)$ *versus* reaction time. The reaction constants values were 29×10^{-3} min^{-1} ($R^2 = 0.99$) and 125×10^{-3} min^{-1} ($R^2 = 0.99$) for the $ZnFe_2O_4$-EG and $ZnFe_2O_4$-BD samples, respectively. Thus, $ZnFe_2O_4$-BD exhibited a rate that was about four times faster than that of $ZnFe_2O_4$-EG, which may associated with its higher surface area. Therefore, the results showed that the $ZnFe_2O_4$-BD sample displayed higher catalytic activity than that of the $ZnFe_2O_4$-EG sample under visible light irradiation. Due to its magnetic property [49], $ZnFe_2O_4$ spinel can be separated and recovered from aqueous solution through a magnetic field for further reutilization. The leaching of Fe ions in the solution was measured at 60 min irradiation for both catalysts. The concentrations of leached Fe were 4.2 and 4.5 mg·L^{-1} for the $ZnFe_2O_4$-BD and $ZnFe_2O_4$-EG catalysts, respectively, which are below the level established by the Brazilian environmental legislation (CONAMA) [50] for discharge in waste effluents, *i.e.*, 15 mg·L^{-1}.

Figure 4. Atomic force microscopy (AFM) of (**a**) $ZnFe_2O_4$-BD and (**b**) $ZnFe_2O_4$-EG.
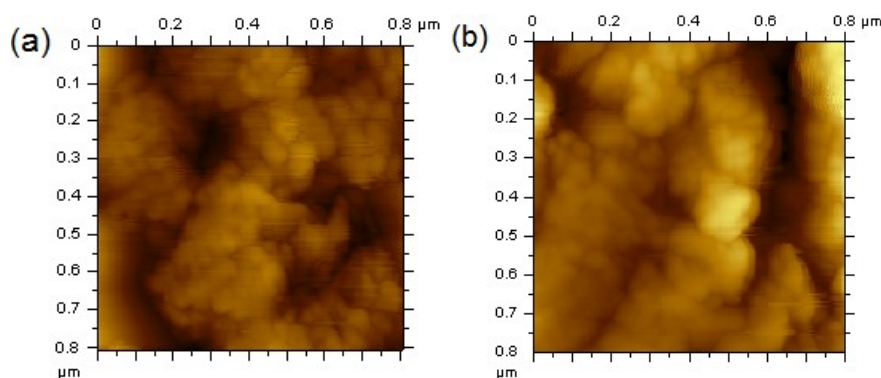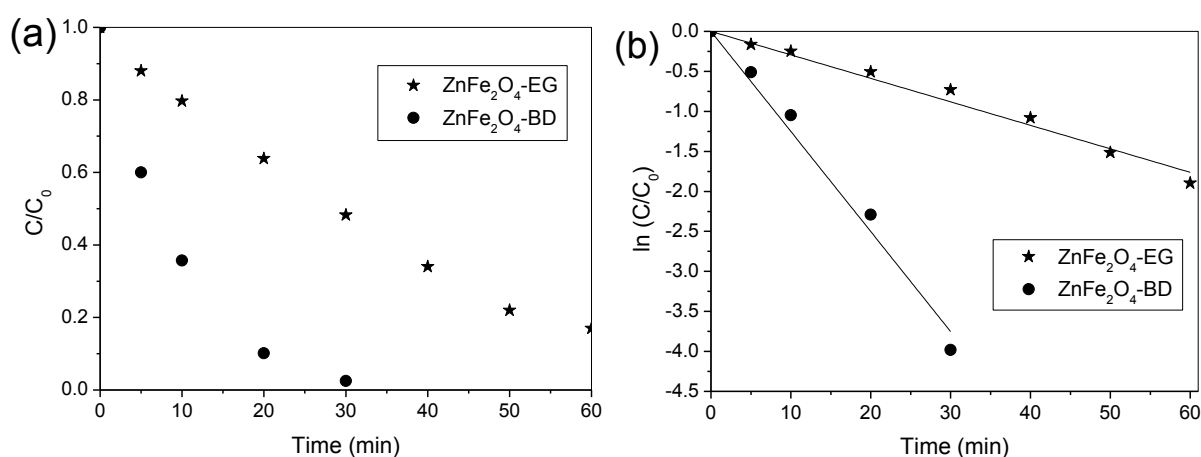

Figure 5. (**a**) Degradation profiles and (**b**) the variation of $\ln(C/C_0)$ of Procion red dye over $ZnFe_2O_4$-EG and $ZnFe_2O_4$-DB. Reaction conditions: Initial H_2O_2 concentration = 0.04 mol·L^{-1}, catalyst amount = 0.5 g, initial dye concentration = 50 mg·L^{-1} and initial pH = 3.0.

4. Conclusions

A solvothermal technique was used to produce $ZnFe_2O_4$ particles using two diol solvents. Results indicated that different physical properties may be found when different solvents are used for the synthesis of $ZnFe_2O_4$ particles. $ZnFe_2O_4$ particles were used as a heterogeneous photo-Fenton catalyst, exhibiting a good catalytic activity towards the degradation of Procion red dye in the presence of H_2O_2/visible light. Due to its greater surface area, $ZnFe_2O_4$-BD had a faster degradation rate compared to that of $ZnFe_2O_4$-EG. The photocatalytic degradation of Procion red dye from aqueous solution in the $ZnFe_2O_4$-visible irradiation-H_2O_2 system followed pseudo first-order kinetics. $ZnFe_2O_4$ catalysts prepared herein presented low iron leaching, and may be easily recovered and separated from aqueous solution with the aid of a magnetic field.

Acknowledgments

Author Contributions

All authors have equally contributed to this work. Edson Luiz Foletto has elaborated the research idea, written and edited this paper. Chayene Gonçalves Anchieta performed the catalytic tests and contributed to the discussion of the experimental results. Adriano Cancelier, Marcio Antonio Mazutti and Raquel Cristine Kuhn have characterized the samples and interpreted their results. Andre Gündel, Sérgio Luiz Jahn and Osvaldo Chiavone-Filho focused on literature survey and on the discussion of results concerning the photo-Fenton reaction.

Conflicts of Interest

The authors declare no conflict of interest.

References

1. Mathew, D.S.; Juang, R.S. An overview of the structure and magnetism of spinel ferrite nanoparticles and their synthesis in microemulsions. *Chem. Eng. J.* **2007**, *129*, 51–65.
2. Pradeep, A.; Priyadharsini, P.; Chandrasekaran, G. Structural, magnetic and electrical properties of nanocrystalline zinc ferrite. *J. Alloy. Compd.* **2011**, *509*, 3917–3923.
3. Fan, G.; Gu, Z.; Yang, L.; Li, F. Nanocrystalline zinc ferrite photocatalysts formed using the colloid mill and hydrothermal technique. *Chem. Eng. J.* **2009**, *155*, 534–541.
4. Chu, X.; Liu, X.; Meng, G. Preparation and gas sensitivity properties of $ZnFe_2O_4$ semiconductors. *Sens. Actuators B Chem.* **1999**, *55*, 19–22.
5. Ahmed, M.A.; Alonso, L.; Palacios, J.M.; Cilleruelo, C.; Abanades, J.C. Structural changes in zinc ferrites as regenerable sorbents for hot coal gas desulfurization. *Solid State Ion.* **2000**, *138*, 51–62.

6. Wan, J.; Jiang, X.; Li, H.; Chen, K. Facile synthesis of zinc ferrite nanoparticles as non-lanthanide T1 MRI contrast agents. *J. Mater. Chem.* **2012**, *22*, 13500–13505.

7. Albuquerque, A.S.; Ardisson, J.D.; Bittencourt, E.; Macedo, W.A.A. Structure and magnetic properties of granular NiZn-ferrite-SiO_2. *Mater. Res.* **1999**, *2*, 235–238.

8. Kumar, G.S.Y.; Naik, H.S.B.; Roy, A.S.; Harish, K.N.; Viswanath, R. Synthesis, optical and electrical properties of $ZnFe_2O_4$ nanocomposites. *Nanotechnol. Nanomater.* **2012**, *2*, doi:10.5772/56169.

9. Mekap, A.; Das, P.R.; Choudhary, R.N.P. Dielectric, magnetic and electrical properties of $ZnFe_2O_4$ ceramics. *J. Mater. Sci. Mater. Electron.* **2013**, *24*, 4757–4763.

10. Gama, A.M.; Rezende, M.C. Complex permeability and permittivity variation of radar absorbing materials based on MnZn ferrite in microwave frequencies. *Mater. Res.* **2013**, *16*, 997–1001.

11. Yelenich, O.V.; Solopan, S.O.; Kolodiazhnyi, T.V.; Dzyublyuk, V.V.; Tovstolytkin, A.I.; Belous, A.G. Magnetic properties and high heating efficiency of $ZnFe_2O_4$ nanoparticles. *Mater. Chem. Phys.* **2014**, *146*, 129–135.

12. Toledo-Antonio, J.A.; Nava, N.; Martinez, M.; Bokhimi, X. Correlation between the magnetism of non-stoichiometric zinc ferrites and their catalytic activity for oxidative dehydrogenation of 1-butene. *Appl. Catal. A Gen.* **2002**, *234*, 137–144.

13. Casbeer, E.; Sharma, V.K.; Li, X.Z. Synthesis and photocatalytic activity of ferrites under visible light: A review. *Sep. Purif. Technol.* **2012**, *87*, 1–14.

14. Liu, L.; Zhang, G.; Wang, L.; Huang, T.; Qin, L. Highly active S-modified $ZnFe_2O_4$ heterogeneous catalyst and its photo-Fenton behavior under UV–visible irradiation. *Ind. Eng. Chem. Res.* **2011**, *50*, 7219–7227.

15. Li, P.; Xu, H.Y.; Li, X.; Liu, W.C.; Li, Y. Preparation and evaluation of a photo-Fenton heterogeneous catalyst: Spinel-typed $ZnFe_2O_4$. *Adv. Mater. Res.* **2012**, *550–553*, 329–335.

16. Wu, J.; Pu, W.; Yang, C.; Zhang, M.; Zhang, J. Removal of benzotriazole by heterogeneous photoelectro-Fenton like process using $ZnFe_2O_4$ nanoparticles as catalyst. *J. Environ. Sci.* **2013**, *25*, 801–807.

17. Sun, Y.; Wang, W.; Zhang, L.; Sun, S.; Gao, E. Magnetic $ZnFe_2O_4$ octahedra: Synthesis and visible light induced photocatalytic activities. *Mater. Lett.* **2013**, *98*, 124–127.

18. Nan, C.; Fan, G.; Fan, J.; Li, F. Template-assisted route to porous zinc ferrite film with enhanced visible-light induced photocatalytic performance. *Mater. Lett.* **2013**, *106*, 5–7.

19. Dom, R.; Subasri, R.; Radha, K.; Borse, P.H. Synthesis of solar active nanocrystalline ferrite, MFe_2O_4 (M: Ca, Zn, Mg) photocatalyst by microwave irradiation. *Solid State Commun.* **2011**, *151*, 470–473.

20. Teixeira, A.M.R.F.; Ogasawara, T.; Nóbrega, M.C.S. Investigation of sintered cobalt-zinc ferrite synthesized by coprecipitation at different temperatures: A relation between microstructure and hysteresis curves. *Mater. Res.* **2006**, *9*, 257–262.

21. Li, Q.; Bo, C.; Wang, W. Preparation and magnetic properties of $ZnFe_2O_4$ nanofibers by coprecipitation—Air oxidation method. *Mater. Chem. Phys.* **2010**, *124*, 891–893.

22. Liu, H.; Guo, Y.; Zhang, Y.; Wu, F.; Liu, Y.; Zhang, D. Synthesis and properties of $ZnFe_2O_4$ replica with biological hierarchical structure. *Mater. Sci. Eng. B* **2013**, *178*, 1057–1061.

23. Jesus, C.B.R.; Mendonça, E.C.; Silva, L.S.; Folly, W.S.D.; Meneses, C.T.; Duque, J.G.S. Weak ferromagnetic component on the bulk $ZnFe_2O_4$ compound. *J. Magn. Magn. Mater*. **2014**, *350*, 47–49.

24. Patil, J.Y.; Nadargi, D.Y.; Gurav, J.L.; Mulla, I.S.; Suryavanshi, S.S. Glycine combusted $ZnFe_2O_4$ gas sensor: Evaluation of structural, morphological and gas response properties. *Ceram. Int*. **2014**, *40*, 10607–10613.

25. Costa, A.C.F.M.; Tortella, E.; Neto, E.F.; Morelli, M.R.; Kiminami, R.H.G.A. Sintering of Ni-Zn ferrite nanopowders by the constant heating rate (CHR) method. *Mater. Res*. **2004**, *7*, 523–528.

26. Dantas, J.; Santos, J.R.D.; Cunha, R.B.L.; Kiminami, R.H.G.A.; Costa, A.C.F.M. Use of Ni-Zn ferrites doped with Cu as catalyst in the transesterification of soybean oil to methyl esters. *Mater. Res*. **2013**, *16*, 625–627.

27. Han, L.; Zhou, X.; Wan, L.; Deng, Y.; Zhan, S. Synthesis of $ZnFe_2O_4$ nanoplates by succinic acid-assisted hydrothermal route and their photocatalytic degradation of rhodamine B under visible light. *J. Environ. Chem. Eng.* **2014**, *2*, 123–130.

28. Blanco-Gutierrez, V.; Climent-Pascual, E.; Torralvo-Fernandez, M.J.; Saez-Puche, R.; Fernandez-Diaz, M.T. Neutron diffraction study and superparamagnetic behavior of $ZnFe_2O_4$ nanoparticles obtained with different conditions. *J. Solid State Chem*. **2011**, *184*, 1608–1613.

29. Banerjee, A.; Bid, S.; Dutta, H.; Chaudhuri, S.; Das, D.; Pradhan, S.K. Microstructural changes and effect of variation of lattice strain on positron annihilation lifetime parameters of zinc ferrite nanocomposites prepared by high enegy ball-milling. *Mater. Res*. **2012**, *15*, 1022–1028.

30. Mohai, I.; Szépvölgyi, J.; Bertóti, I.; Mohai, M.; Gubicza, J.; Ungár, T. Thermal plasma synthesis of zinc ferrite nanopowders. *Solid State Ion*. **2001**, *141–142*, 163–168.

31. Cao, Y.; Jia, D.; Hu, P.; Wang, R. One-step room-temperature solid-phase synthesis of $ZnFe_2O_4$ nanomaterials and its excellent gas-sensing property. *Ceram. Int.* **2013**, *39*, 2989–2994.

32. Manikandan, A.; Kennedy, L.J.; Bououdina, M.; Vijaya, J.J. Synthesis, optical and magnetic properties of pure and Co-doped $ZnFe_2O_4$ nanoparticles by microwave combustion method. *J. Magn. Magn. Mater*. **2014**, *349*, 249–258.

33. Köseoğlu, Y.; Baykal, A.; Toprak, M.S.; Gözüak, F.; Başaran, A.C.; Aktaş, B. Synthesis and characterization of $ZnFe_2O_4$ magnetic nanoparticles via a PEG-assisted route. *J. Alloy. Compnd.* **2008**, *462*, 209–213.

34. Oliver, S.A. Localized spin canting in partially inverted $ZnFe_2O_4$ fine powders. *Phys. Rev. B* **1999**, *60*, 3400–3405.

35. Cabañas, A.; Poliakoff, M. The continuous hydrothermal synthesis of nano-particulate ferrites in near critical and supercritical water. *J. Mater. Chem.* **2001**, *11*, 1408–1416.

36. Shen, Y.; Li, X.; Zhao, Q.; Hou, Y.; Tade, M.; Liu, S. Facile synthesis and characterization of $ZnFe_2O_4/\alpha$-Fe_2O_3 composite hollow nanospheres. *Mater. Res. Bull.* **2011**, *46*, 2235–2239.

37. Li, X.; Hou, Y.; Zhao, Q.; Wang, L. A general, one-step and template-free synthesis of sphere-like zinc ferrite nanostructures with enhanced photocatalytic activity for dye degradation. *J. Colloid Interface Sci.* **2011**, *358*, 102–108.

38. Kuai, S.; Zhang, Z.; Nan, Z. Synthesis of Ce^{3+} doped $ZnFe_2O_4$ self- assembled clusters and adsorption of chromium(VI). *J. Hazard. Mater*. **2013**, *250–251*, 229–237.

39. Cullity, B.D.; Stock, S.R. *Elements of X-ray Diffraction*, 3rd ed.; Prentice-Hall Inc.: Upper Saddle River, NJ, USA, 2001.

40. Liu, X.; Zheng, H.; Yong, L.; Zhang, W. Factors on the separation of photogenerated charges and the charge dynamics in oxide/$ZnFe_2O_4$ composites. *J. Mater. Chem. C* **2013**, *1*, 329–337.

41. Soon, A.N.; Hameed, B.H. Degradation of Acid Blue 29 in visible light radiation using iron modified mesoporous silica as heterogeneous Photo-Fenton catalyst. *Appl. Catal. A Gen.* **2013**, *450*, 96–105.

42. Yuan, S.-J.; Dai, X.-H. Facile synthesis of sewage sludge-derived mesoporous material as anefficient and stable heterogeneous catalyst for photo-Fenton reaction. *Appl. Catal. B Environ.* **2014**, *154–155*, 252–258.

43. Babuponnusami, A.; Muthukumar, K. A review on Fenton and improvements to the Fenton process for wastewater treatment. *J. Environ. Chem. Eng.* **2014**, *2*, 557–572.

44. Köseoğlu, Y.; Baykal, A.; Gözüak, F.; Kavas, H. Structural and magnetic properties of $Co_xZn_{1-x}Fe_2O_4$ nanocrystals synthesized by microwave method. *Polyhedron* **2009**, *28*, 2887–2892.

45. Hou, Y.; Li, X.; Zhao, Q.; Chen, G. $ZnFe_2O_4$ multi-porous microbricks/graphene hybrid photocatalyst: Facile synthesis, improved activity and photocatalytic mechanism. *Appl. Catal. B Environ.* **2013**, *142–143*, 80–88.

46. Mizukami, F.; Kiyozumi, Y.; Sano, T.; Niwa, S.I.; Toba, M.; Shin, S. Effect of solvent diols and ligands on the properties of sol-gel alumina-silicas. *J. Sol-Gel Sci. Technol.* **1998**, *13*, 1027–1031.

47. Borhan, A.I.; Samoila, P.; Hulea, V.; Iordan, A.R.; Palamaru, M.N. Effect of Al^{3+} substituted zinc ferrite on photocatalytic degradation of orange I azo dye. *J. Photochem. Photobiol. A Chem.* **2014**, *279*, 17–23.

48. Anchieta, C.G.; Sallet, D.; Foletto, E.L.; Silva, S.S.; Chiavone-Filho, O.; Nascimento, C.A.O. Synthesis of ternary zinc spinel oxides and their application in the photodegradation of organic pollutant. *Ceram. Inter.* **2014**, *40*, 4173–4178.

49. Blanco-Gutierrez, V.; Saez-Puche, R.; Torralvo-Fernandez, M.J. Superparamagnetism and interparticle interactions in $ZnFe_2O_4$ nanocrystals. *J. Mater. Chem.* **2012**, *22*, 2992–3003.

50. National Council on Environmental (Brazil). Available online: http://www.mma.gov.br/port/conama (accessed on 6 July 2014).